Supporting Information

Microsolvation of the Acetanilide Cation (AA^+) in a Nonpolar Solvent: IR Spectra of AA^+-L_n clusters (L=He, Ar, N_2; n≤10)

by

Matthias Schmies,[a] Alexander Patzer,[a] Markus Schütz,[a] Mitsuhiko Miyazaki,[b] Masaaki Fujii,[b] and Otto Dopfer*[a]

[a] Institut für Optik und Atomare Physik, Technische Universität Berlin, Hardenbergstr. 36, 10623 Berlin Germany

* Fax: (+49) 30-31423018, E-mail: dopfer@physik.tu-berlin.de

[b] Chemical Resources Laboratory, Tokyo Institute of Technology, Yokohama 226-8503, Japan

Figure S1. Highest occupied molecular orbitals (HOMO, HOMO-1, LUMO) of t-AA^+ and c-AA^+ calculated at the M06-2X/aug-cc-pVTZ level.

Figure S2. NBO charge distribution (in 10^{-3} e) of t-AA^+ and c-AA^+ in the cation ground electronic state (D_0) evaluated at the M06-2X/aug-cc-pVTZ level.

Figure S3. IRPD spectra of AA^+-Ar_n with n≤7 in the C-H and N-H stretch range recorded in the dominant fragment channel, indicted as n-m. For comparison, the IRPD spectrum of AA^+-He is plotted as well. The positions of the transitions for n=1 are listed in Table 2 along with their vibrational and isomer assignments. The origin of the transition X is unclear. It may arise from isobaric contaminations, i.e. ions with the same mass but different composition.

Figure S4. IRPD spectra of AA^+-$(N_2)_n$ with n≤10 in the C-H and N-H stretch range recorded in the dominant fragment channel, indicted as n-m. For comparison, the IRPD spectrum of AA^+-He is plotted as well. The positions of the transitions for n=1 are listed in Table 2 along with their vibrational and isomer assignments. The origin of the transitions labelled with X-Z is unclear. They may arise from isobaric contaminations, i.e. ions with the same mass but different composition.

Figure S5. Experimental IR spectra of AA^+-Ar and t-AA (taken from Miyazaki et al, PCCP 11, 2009, 6098) in the C-H and N-H stretch range are compared to linear IR absorption spectra of t-AA^+ and t-AA calculated at the M06-2X/aug-cc-pVTZ level.

Figure S6. IRPD spectra of AA^+-Ar_n with n≤4 in the fingerprint range recorded in the dominant fragment channels, indicted as n-m. The positions of the transitions for n=1 are listed in Table 2 along with their vibrational and isomer assignments. For AA^+-Ar, spectra with high and low detector sensitivity are shown. The one with high detector sensitivity shows weak bands but the strong transitions near 1530 cm^{-1} are saturated.

Figure S7. IRPD spectra of AA^+-$(N_2)_n$ with n≤3 in the fingerprint range recorded in the dominant fragment channels, indicted as n-m. The positions of the transitions for n=1 are listed in Table 2 along with their vibrational and isomer assignments.

Figure S8. Experimental IR spectra of AA^+-Ar and t-AA (taken from Miyazaki et al, PCCP 11, 2009, 6098) in the fingerprint range are compared to linear IR absorption spectra of t-AA^+ and t-AA calculated at the M06-2X/aug-cc-pVTZ level.

Figure S9. Expanded view of the IRPD spectra of AA^+-L_n with L=Ar (n≤4) and N_2 (n≤3) recorded in the amide II range are compared to the linear IR absorption spectra calculated for t-AA^+, t-AA^+-Ar(H), and t-AA^+-N_2(H) at the M06-2X/aug-cc-pVTZ level. The positions of the transitions for n=1 are listed in Table 2 along with their vibrational and isomer assignments.

Figure S10. IRPD spectra of AA^+-Ar_n with n=1 and 2 when the cluster ions are generated either by one-color two-photon (1+1) REMPI of the neutral AA-Ar_n dimers (blue) or by EI (red). The REMPI-IR spectra are obtained by isomer-selective resonant ionization of t-AA-Ar(nπ) via their S_1 origins with substantial ionization excess energy and subsequent IRPD at a delay of 50 ns. The REMPI-IR spectra (taken from Sakota et al, J. Phys. Chem. A, 115, 2011, 626), display a systematic redshift of ~7 cm^{-1} compared to the EI-IR spectra which probably arise from calibration issues in the REMPI-IR study.

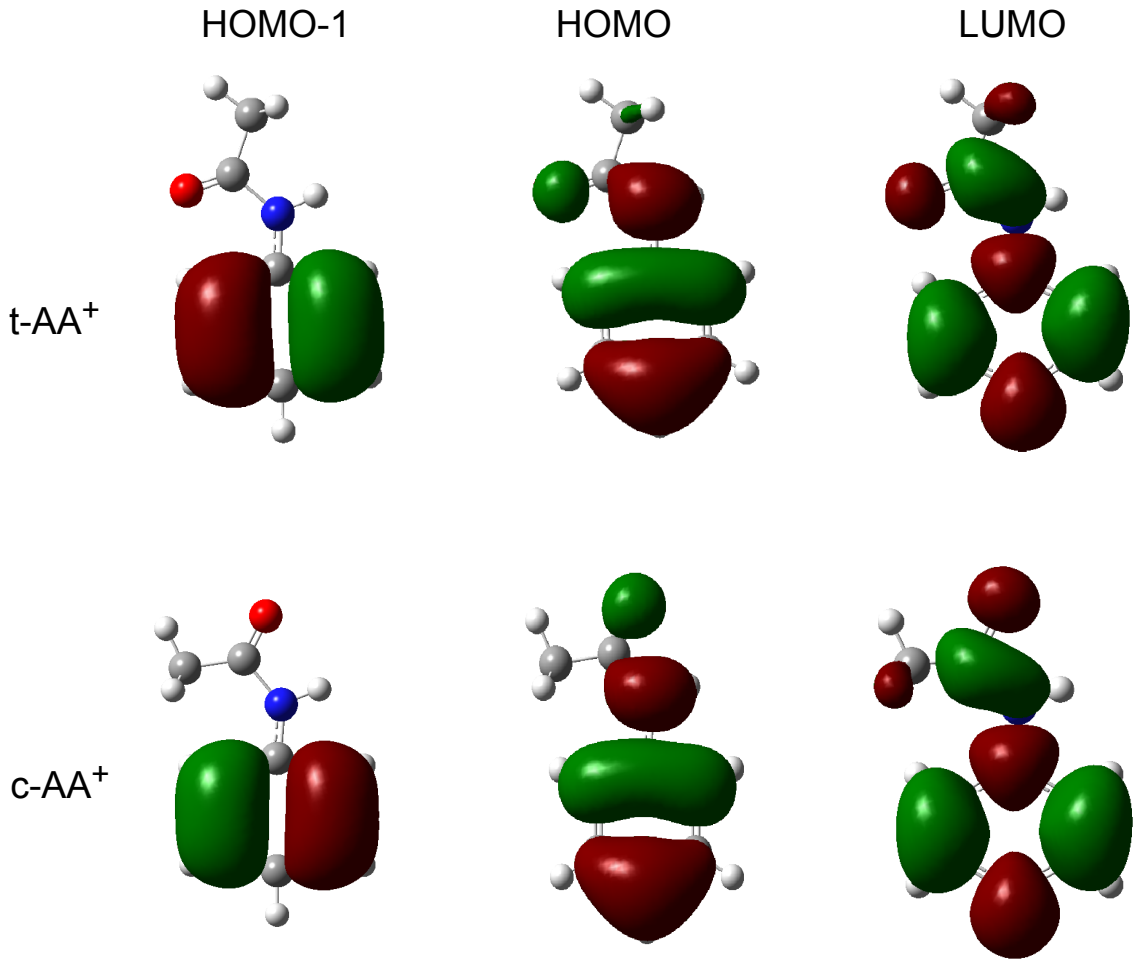

Figure S1

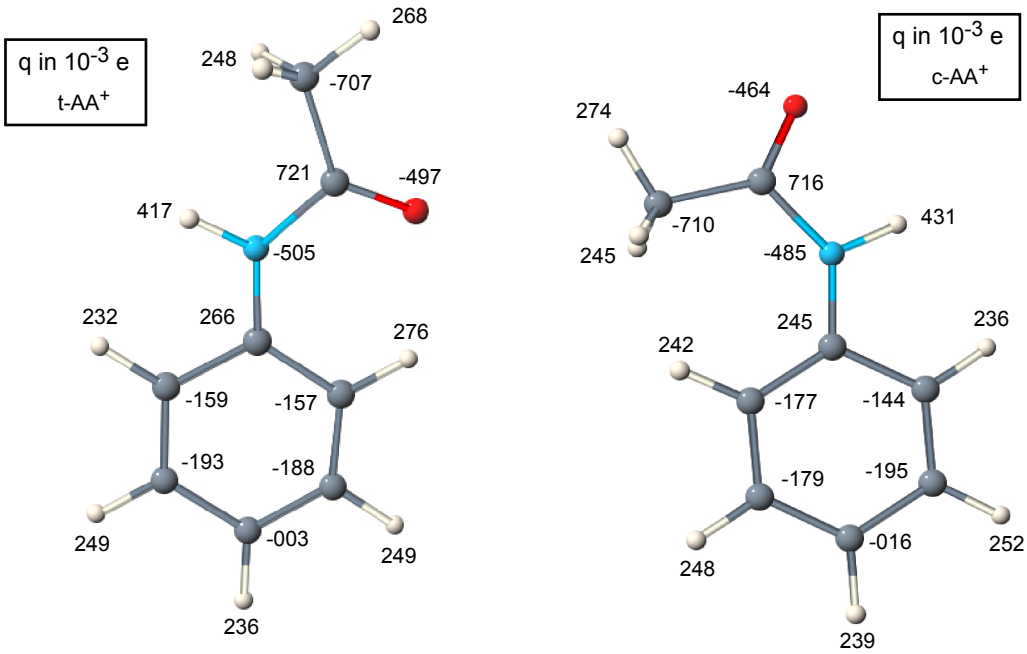
q in 10^{-3} e
t-AA$^+$
268
248
-707
721
-497
417
-505
232
266
276
-159
-157
-193
-188
249
-003
249
236
q in 10^{-3} e
c-AA$^+$
-464
274
716
-710
431
245
-485
245
236
242
-177
-144
-179
-195
248
-016
252
239

Figure S2

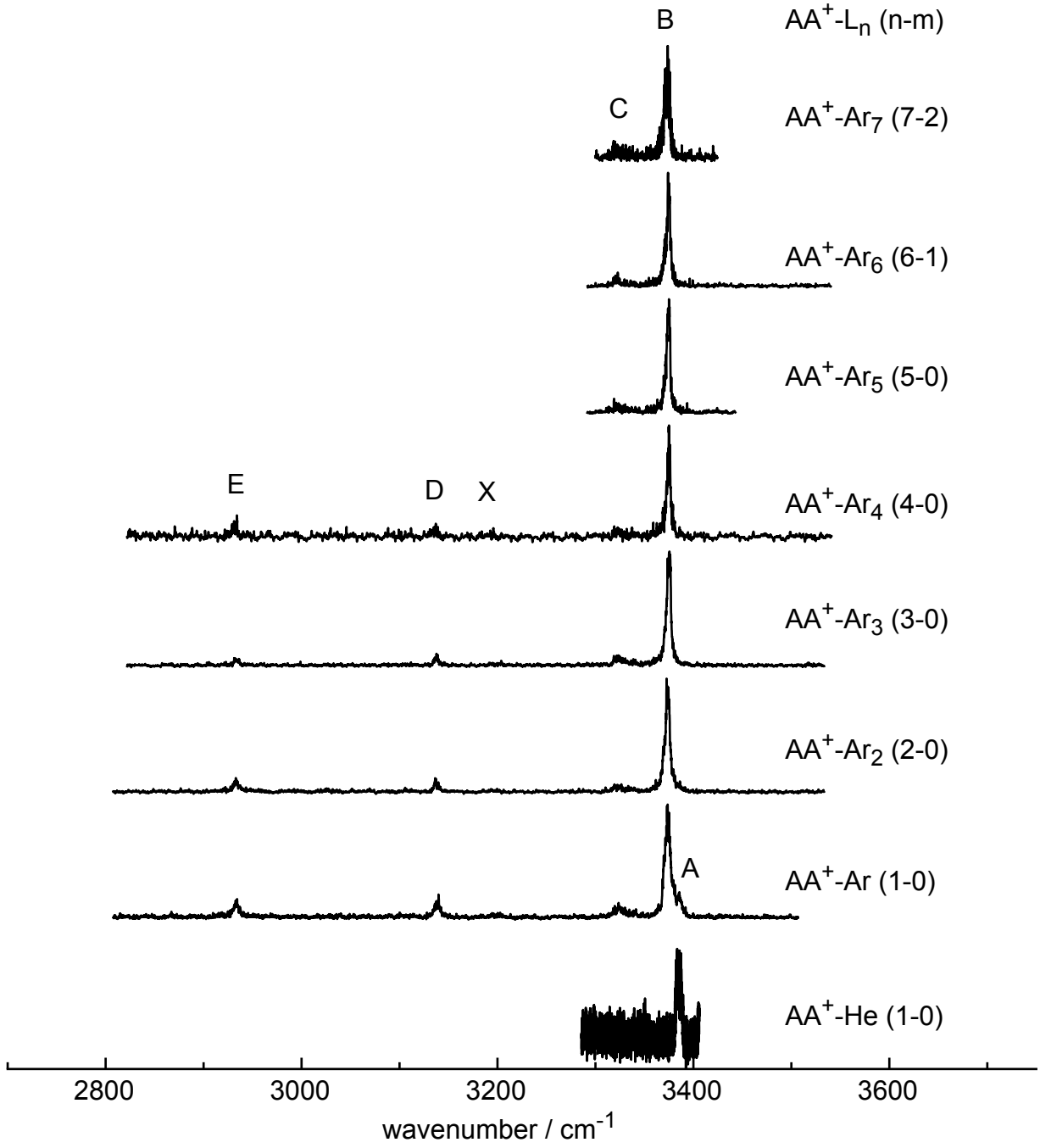
B
AA+-Ln (n-m)
C
AA+-Ar7 (7-2)
AA+-Ar6 (6-1)
AA+-Ar5 (5-0)
E
D
X
AA+-Ar4 (4-0)
AA+-Ar3 (3-0)
AA+-Ar2 (2-0)
A
AA+-Ar (1-0)
AA+-He (1-0)
2800
3000
3200
3400
3600
wavenumber / cm-1

Figure S3

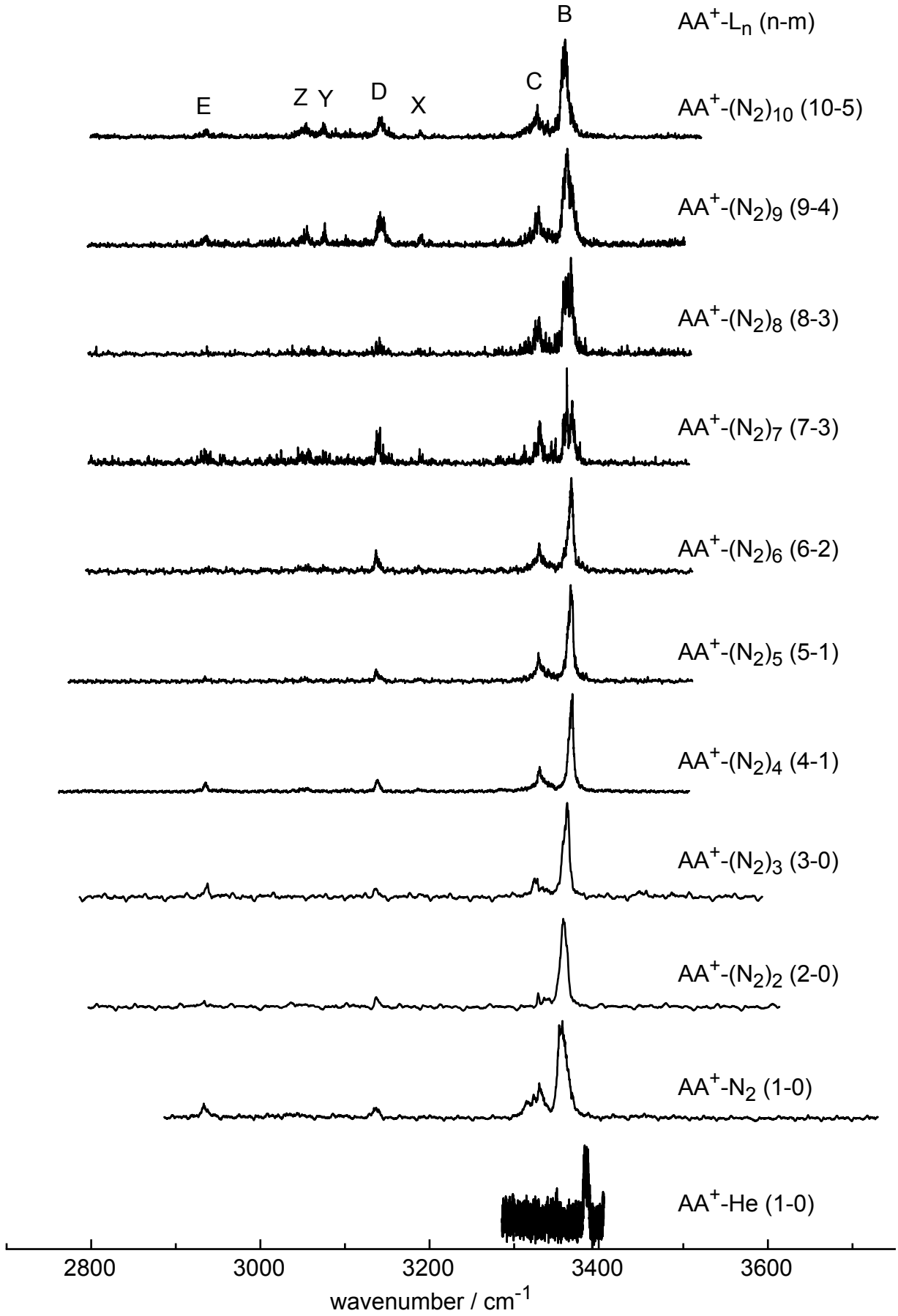
AA+-Ln (n-m)
B
C
E
Z Y
D
X
AA+-(N2)10 (10-5)
AA+-(N2)9 (9-4)
AA+-(N2)8 (8-3)
AA+-(N2)7 (7-3)
AA+-(N2)6 (6-2)
AA+-(N2)5 (5-1)
AA+-(N2)4 (4-1)
AA+-(N2)3 (3-0)
AA+-(N2)2 (2-0)
AA+-N2 (1-0)
AA+-He (1-0)
2800
3000
3200
3400
3600
wavenumber / cm-1

Figure S4

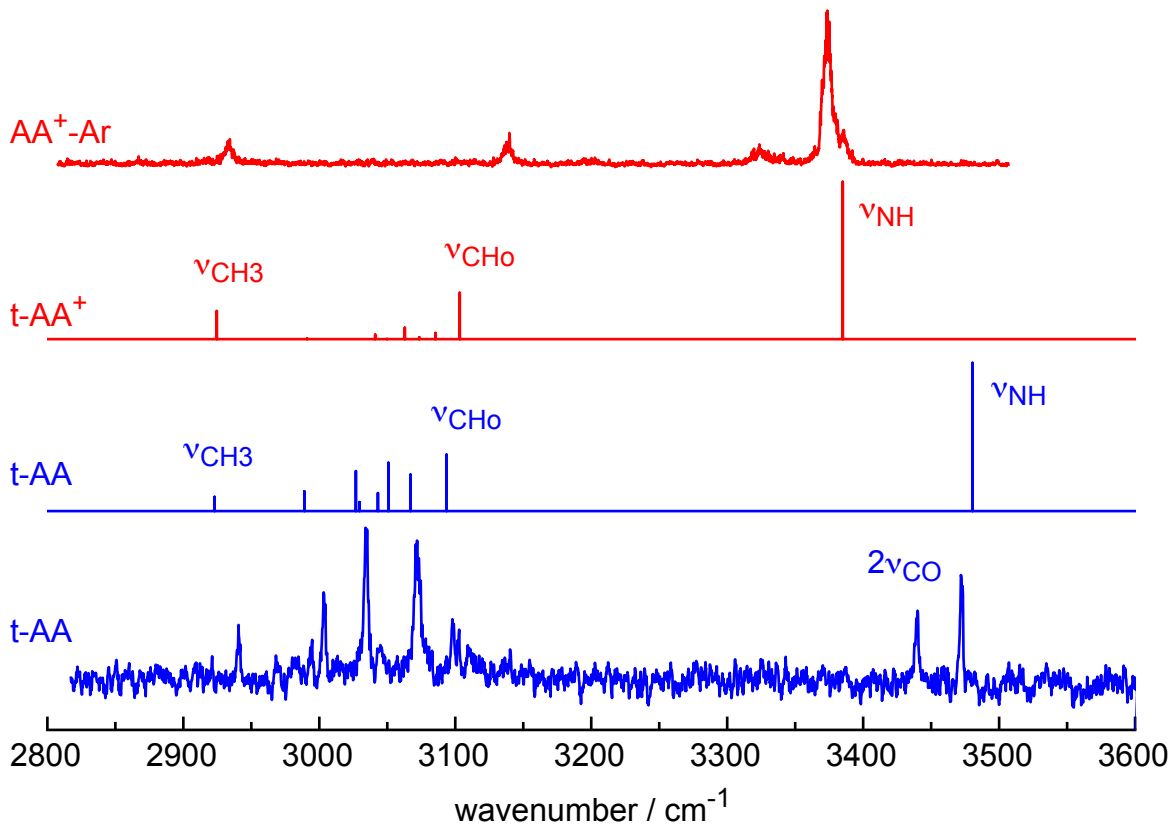
AA+-Ar
t-AA+
νNH
νCHo
νCH3
t-AA
νNH
νCHo
νCH3
t-AA
2νCO
2800
2900
3000
3100
3200
3300
3400
3500
3600
wavenumber / cm-1

Figure S5

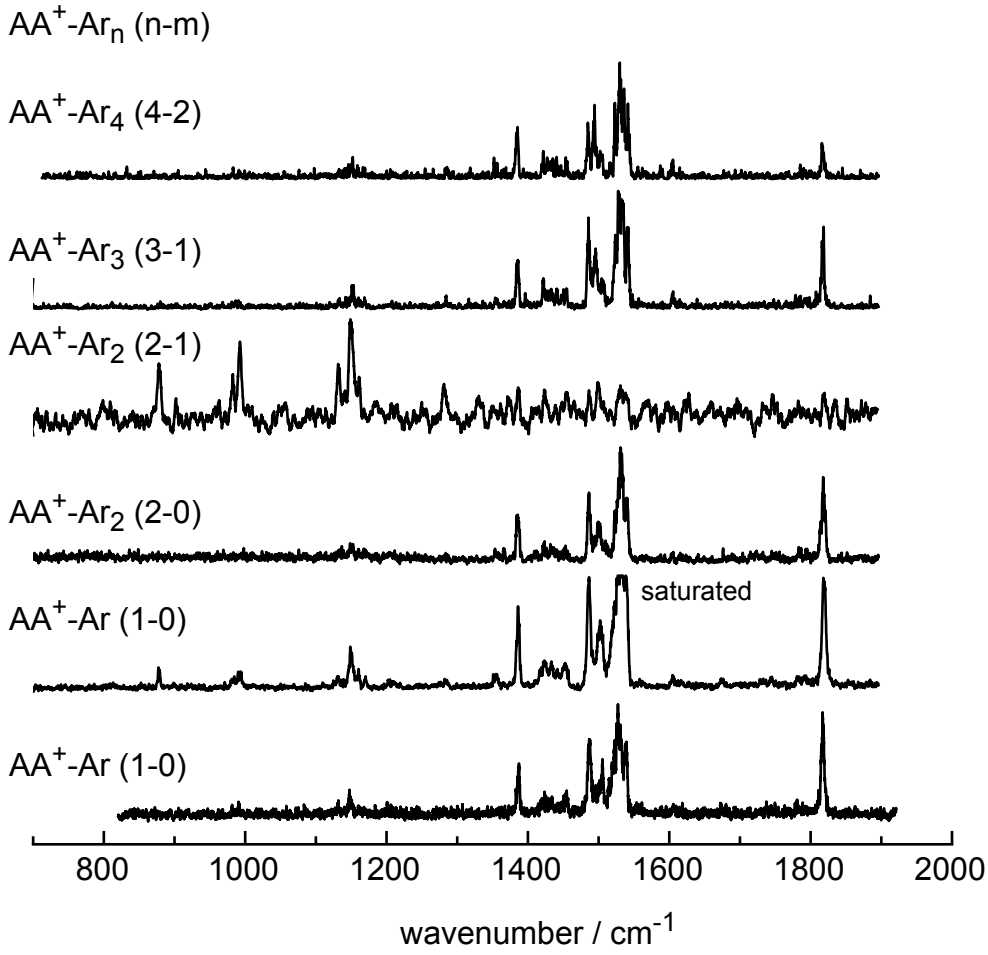
AA+-Arn (n-m)
AA+-Ar4 (4-2)
AA+-Ar3 (3-1)
AA+-Ar2 (2-1)
AA+-Ar2 (2-0)
AA+-Ar (1-0)
saturated
AA+-Ar (1-0)
800
1000
1200
1400
1600
1800
2000
wavenumber / cm-1

Figure S6

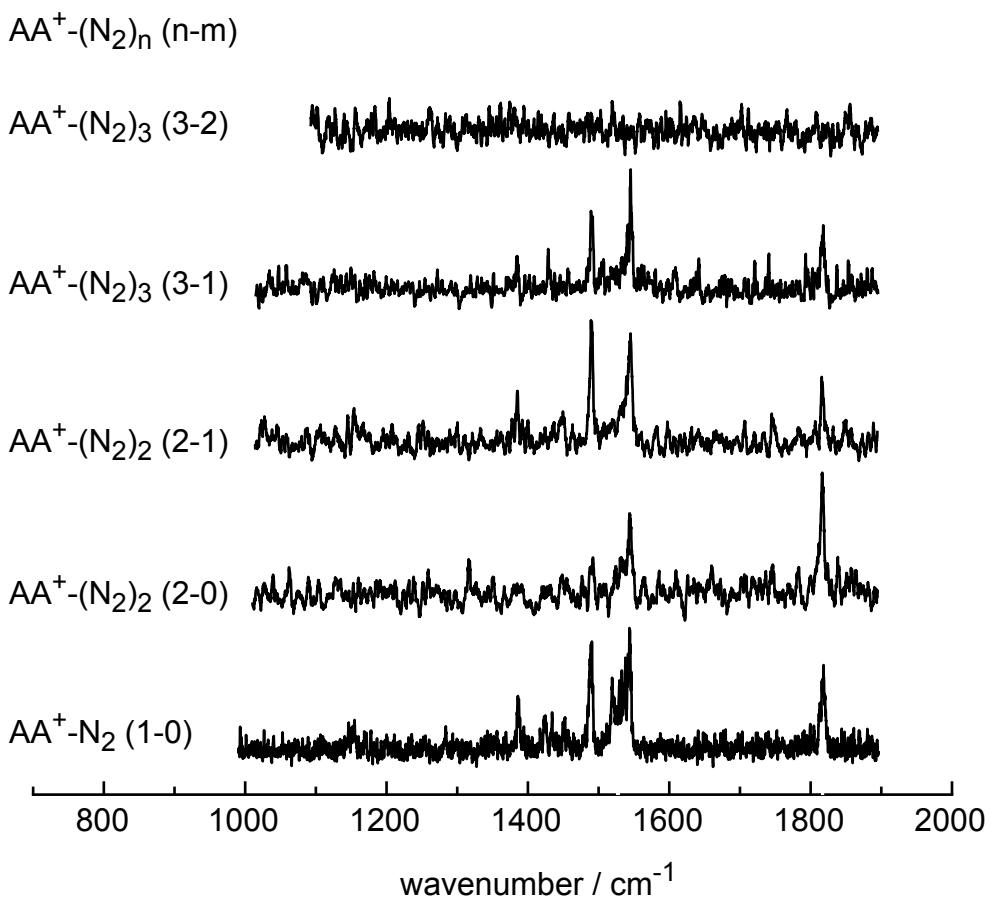
AA+-(N2)n (n-m)
AA+-(N2)3 (3-2)
AA+-(N2)3 (3-1)
AA+-(N2)2 (2-1)
AA+-(N2)2 (2-0)
AA+-N2 (1-0)
800
1000
1200
1400
1600
1800
2000
wavenumber / cm-1

Figure S7

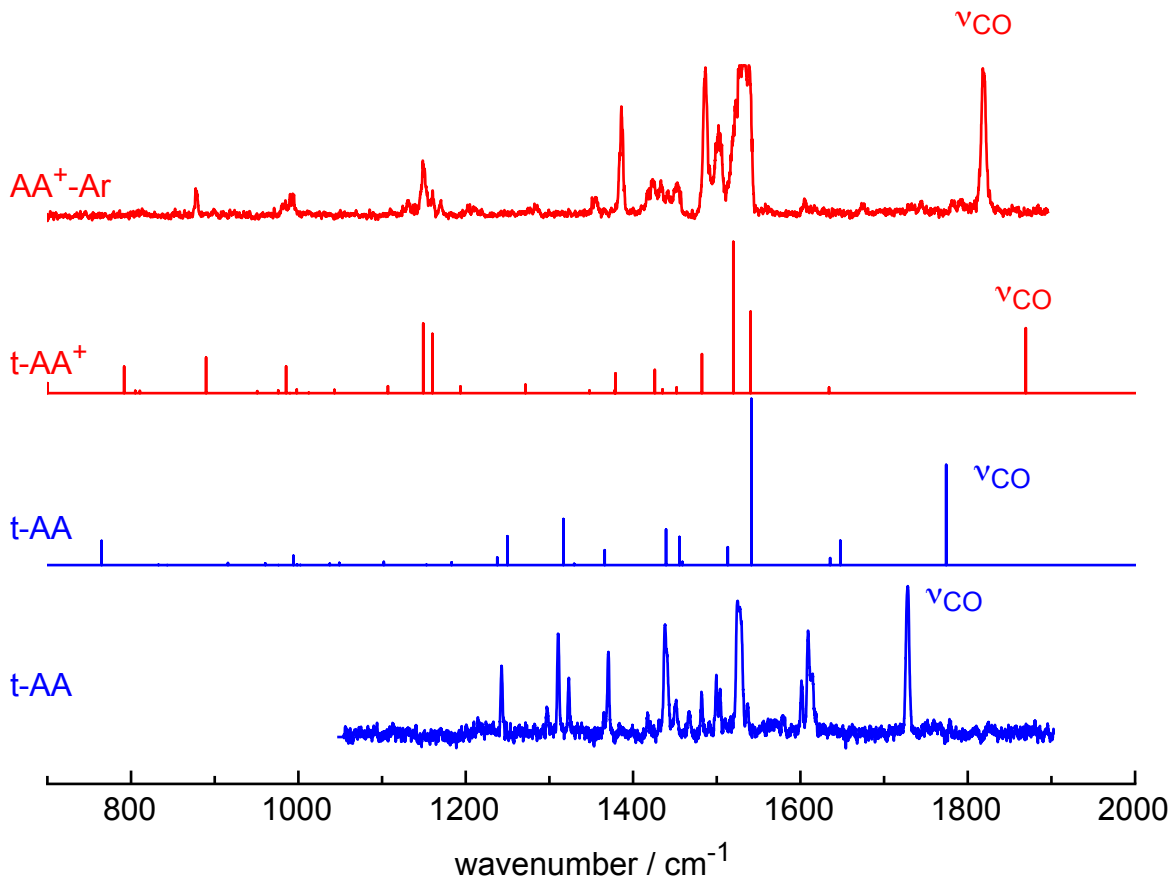
νCO
AA+-Ar
νCO
t-AA+
νCO
t-AA
νCO
t-AA
800
1000
1200
1400
1600
1800
2000
wavenumber / cm-1

Figure S8

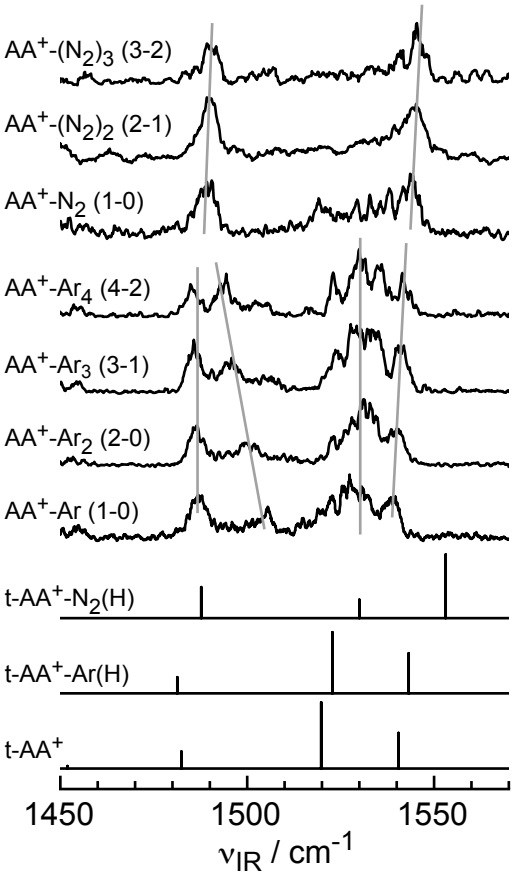
AA+-(N2)3 (3-2)
AA+-(N2)2 (2-1)
AA+-N2 (1-0)
AA+-Ar4 (4-2)
AA+-Ar3 (3-1)
AA+-Ar2 (2-0)
AA+-Ar (1-0)
t-AA+-N2(H)
t-AA+-Ar(H)
t-AA+
1450
1500
1550
νIR / cm-1

Figure S9

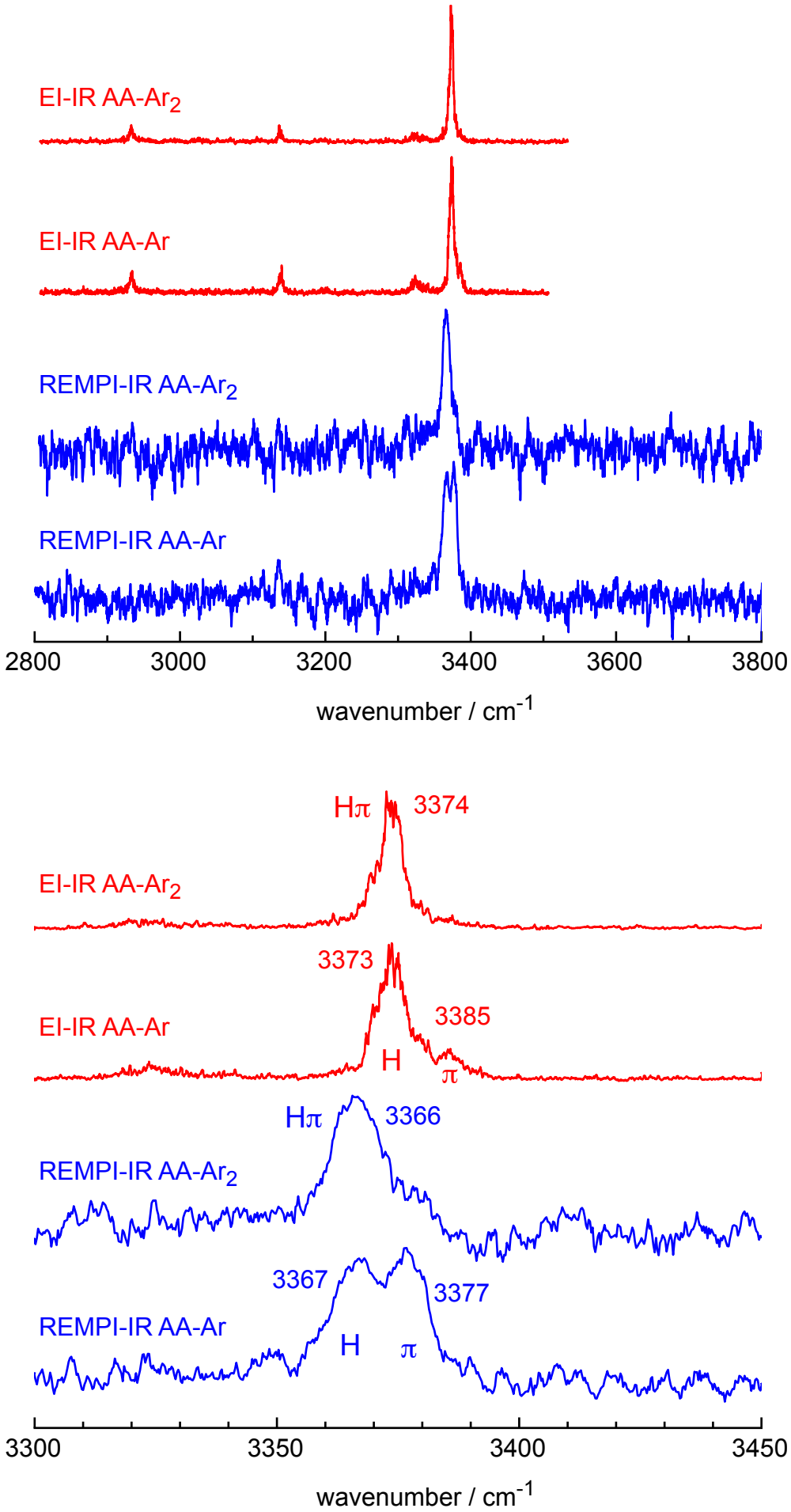
EI-IR AA-Ar2
EI-IR AA-Ar
REMPI-IR AA-Ar2
REMPI-IR AA-Ar
2800
3000
3200
3400
3600
3800
wavenumber / cm-1
Hπ
3374
EI-IR AA-Ar2
3373
3385
EI-IR AA-Ar
H
π
Hπ
3366
REMPI-IR AA-Ar2
3367
3377
REMPI-IR AA-Ar
H
π
3300
3350
3400
3450
wavenumber / cm-1

Figure S10